Nano Energy 30 (2016) 630–638

Contents lists available at ScienceDirect

Nano Energy

journal homepage: www.elsevier.com/locate/nanoen

Enhanced thermoelectric performance of solution-derived bismuth telluride based nanocomposites via liquid-phase Sintering

Chaohua Zhang[a], Maria de la Mata[b], Zhong Li[c], Francisco J. Belarre[b], Jordi Arbiol[b,d], Khiam Aik Khor[c], Dario Poletti[e], Beibei Zhu[f], Qingyu Yan[f], Qihua Xiong[a,*]

[a] Division of Physics and Applied Physics, School of Physical and Mathematical Science, Nanyang Technological University, 637371 Singapore, Singapore
[b] Catalan Institute of Nanoscience and Nanotechnology (ICN2), CSIC and the Barcelona Institute of Science and Technology (BIST), Campus UAB, Bellaterra, Barcelona 08193, Catalonia, Spain
[c] School of Mechanical and Aerospace Engineering, Nanyang Technological University, 639798 Singapore, Singapore
[d] ICREA, Pg. Lluís Companys 23, 08010 Barcelona, Catalonia, Spain
[e] Singapore University of Technology and Design, 8 Somapah Road, 487372 Singapore, Singapore
[f] School of Materials Science and Engineering, Nanyang Technological University, 639798 Singapore, Singapore

ARTICLE INFO

Keywords:
Thermoelectric materials
Nanocomposites
Bottom-up
Liquid-phase sintering
Bismuth telluride

ABSTRACT

Bismuth telluride based thermoelectric materials show great promise in electricity generation from waste heat and solid-state refrigeration, but improving their conversion efficiency with economical approaches for widespread use remains a challenge. An economical facile bottom-up approach has been developed to obtain nanostructured powders, which are used to build bulk thermoelectric materials. Using excess tellurium as sacrificial additive to enable liquid-phase sintering in the spark plasma sintering process, the lattice and bipolar contributions to the thermal conductivity are both greatly reduced without compromising too much the power factor, which leads to the achievement of high figure of merit (ZT) in both n-type and p-type bismuth telluride based nanocomposites. The ZT values are 1.59 ± 0.16 for p-type $Bi_{0.5}Sb_{1.5}Te_3$ and 0.98 ± 0.07 for n-type $Bi_2Te_{2.7}Se_{0.3}$ at 370 K, which are significantly high for bottom-up approaches. These results demonstrate that solution-chemistry approaches as facile, scalable and low-energy-intensive ways to achieve nanopowders, combined with liquid-phase sintering process, can open up great possibilities in developing high-performance low-price thermoelectric bulk nanocomposites.

1. Introduction

Power generation by converting waste heat into useful electricity and cryogen-free solid-state refrigeration are the two major applications for thermoelectric materials [1], which are significant for combating the energy and global warming challenges. Improving the conversion efficiency of thermoelectric materials and developing economical materials and preparing methods are crucial for the widespread use of thermoelectric products [2]. The efficiency of thermoelectric materials is determined by the materials' dimensionless figure of merit (ZT), where $ZT=(S^2/\rho\kappa)T=(PF/\kappa)T$, and S, ρ, κ, T, PF are the Seebeck coefficient, electrical resistivity, thermal conductivity, absolute temperature, and power factor, respectively. Nanostructuring process has been widely proposed to enhance the ZT value of thermoelectric materials by reducing the thermal conductivity without significantly depressing the power factor [3–10]. Generally, nanostructuring processes to bulk thermoelectric materials can be divided into two steps: producing nanostructured powders and sintering powders to bulk composite materials. Top-down approaches using bulk ingots as starting materials like ball-milling [6,11] and melt-spinning [9,12] are widely used to obtain nanostructured powders for ZT-improved bulk materials. Bottom-up approaches from chemical precursors like chemical solution synthesis are another facile, scalable and low-energy-intensive ways to achieve nanostructured powders [13], which thus exhibit considerable promise for fabricating commercial thermoelectric devices at low cost if their ZT values are competitively as high as those top-down processed materials.

Among the big family of thermoelectric materials in all temperature ranges, bismuth telluride (Bi_2Te_3)-based materials (like p-type $Bi_xSb_{2-x}Te_3$ and n-type $Bi_2Te_{3-y}Se_y$) are the most widely-used thermoelectric materials near room temperature region [14]. Commercial Bi_2Te_3-based ingots are prepared by the solid solution alloying method [15], whose ZT peaks have remained at about 1 near room temperature for nearly 50 years. There have been consecutive efforts to improve

* Corresponding author.
E-mail address: Qihua@ntu.edu.sg (Q. Xiong).

http://dx.doi.org/10.1016/j.nanoen.2016.10.056
Received 5 September 2016; Received in revised form 23 October 2016; Accepted 28 October 2016
Available online 30 October 2016

their ZT values by nanostructuring process since the start of this century [6,7,9,10,12,16–19]. For p-type $Bi_xSb_{2-x}Te_3$, ZT peaks > 1.4 around 370–390 K have been achieved using the ball-milling [6] and melt-spinning process [12]. Recently, a higher ZT peak value ~1.86 near 320 K for p-type bulk $Bi_{0.5}Sb_{1.5}Te_3$ has been achieved by a modified melt-spinning process with excess tellurium as sacrificial additive [9]. The ZT improvement of n-type bulk $Bi_2Te_{3-y}Se_y$ is still limited, whose highest recorded ZT value is still around 1.1–1.2 in the range 350–400 K by ball-milling [19] and hot-deformation process [20]. Various bottom-up solution synthesis methods have also been reported to scale up these nanostructured Bi_2Te_3-based materials [7,18,21–42], but resultant composites usually show much lower ZT values compared with the ones made by top-down methods. The achieved ZT value of both n-type and p-type Bi_2Te_3-based materials varies much between different bottom-up chemistry approaches, which ranges from 0.04 [35] to 1.1 [7], and most of them are lower than 1 in the temperature range 300–400 K [18,21–34,36]. The high electrical resistivity and low power factor are the main obstacles for achieving high ZT in those solution-synthesis samples even though their thermal conductivity can be greatly reduced [13]. Reducing the thermal conductivity without compromising much of the power factor remains a challenge for bottom-up chemistry approaches.

Liquid-phase sintering (LPS) is a widely used process for engineering materials [43], which involves the sintering under conditions where a wetting liquid exists between solid grains. LPS has been used to enhance the thermoelectric performance of top-down approach derived p-type $Bi_{0.5}Sb_{1.5}Te_3$ recently [9]. It would be significant for the widespread use of Bi_2Te_3 based thermoelectric products if LPS process can also work for the bottom-up derived samples and n-type $Bi_2Te_{3-y}Se_y$ samples as well.

In this study, we report that high-thermoelectric performance of p-type $Bi_{0.5}Sb_{1.5}Te_3$ and n-type $Bi_2Te_{2.7}Se_{0.3}$ nanobulk materials can be realized by the bottom-up solution-synthesis and LPS-related spark-plasma-sintering approach, by introducing excess tellurium in the chemical synthesis. The excess tellurium as sacrificial additive to enable LPS process is effective for reducing the thermal conductivity without compromising too much the power factor. ZT values as high as 1.59 ± 0.16 for p-type $Bi_{0.5}Sb_{1.5}Te_3$ and 0.98 ± 0.07 for n-type $Bi_2Te_{2.7}Se_{0.3}$ are obtained at 370 K, much higher than other reports using chemical approaches, opening up great possibilities for the commercial use of chemically scalable bulk nanocomposites in solid-state refrigeration and low-temperature power generation.

2. Materials and methods

2.1. Chemical solution synthesis of nanostructured powders

To synthesize 4 mmol Te-excess-$Bi_{0.5}Sb_{1.5}Te_3$ mixture, 15 mmol potassium tellurite monohydrate, 2 mmol bismuth acetate, 6 mmol antimony acetate, 40 mmol potassium hydroxide and 0.4 g Polyvinylpyrrolidone (PVP, average M_w~55,000) were dissolved or dispersed in the 160 ml diethylene glycol (DEG) solvent. After that, 0.4 g L-cysteine was added to the mixed solution. Then the solution was heated at the boiling temperature of DEG (~ 240 °C) for 3 h. To synthesize 4 mmol Te-excess-$Bi_2Te_{2.7}Se_{0.3}$ mixture, 13.9 mmol potassium tellurite monohydrate, 1.2 mmol potassium selenite, 8 mmol bismuth acetate, 40 mmol potassium hydroxide and 0.4 g PVP were dissolved in the 160 ml ethylene glycol (EG) solvent. Then the mixed solution was heated at the boiling temperature of EG (~ 190 °C) for 3 h. After reaction, the black precipitates were washed in acetone and isopropanol with the assistance of sonication and centrifuging. After that, those precipitates were dried in a dry cabinet at room temperature for about one day and ground into fine powders.

2.2. Preparation of thermoelectric bulk samples

Our nanostructured n-type $Bi_2Te_{2.7}Se_{0.3}$ and p-type $Bi_{0.5}Sb_{1.5}Te_3$ bulk samples (n-Nano and p-Nano) were produced by spark plasma sintering (SPS) of those synthesized powders at 460 °C for 3 min with an applied pressure of 60 MPa. The commercial n-type $Bi_2Te_{2.7}Se_{0.3}$ and p-type $Bi_{0.5}Sb_{1.5}Te_3$ ingots (n-Ingot and p-Ingot) as comparing materials were purchased from the company of Thermonamic Electronics (Jiangxi) Corp., Ltd. Using the traditional Archimedes method, the density of n-Ingot and p-Ingot were measured to be 7.75 and 6.86 g/cm^3 respectively. And the densities of our SPS yielded n-Nano and p-Nano were about 83–91%, 86–90% of that of n-Ingot and p-Ingot respectively. After SPS, our pellet-like bulk samples were cut to bars with length ~10 mm, width ~2.5 mm and thickness ~1 mm. The commercial ingot samples were cut into bars along the cleavage directions having the largest ZT. To make the final samples for thermoelectric measurements, all the bars were polished with sandpapers firstly (with grit size from P400, P800, P1200 to P2400), and then four-probe leads were attached to the bars by applying the silver-filled H20E-HC epoxy.

2.3. X-ray diffraction and electron microscopy

X-ray diffraction (XRD) patterns were performed using a Bruker D8 advance diffractometer with Cu K_α radiation (λ=0.15404 nm) in the locked couple mode. Scanning electron microscopy (SEM, JEOL 7100 F) were taken for morphology characterizations. For (scanning) transmission electron microscopy ((S)TEM) characterizations, nanobulk samples were cut for planar and cross-section view with a diamond wire precision saw and then mechanically thinned by using diamond films. The final polishing step included conventional ion milling in a GATAN PIPS. The samples were then studied by (S)TEM in a FEI Tecnai F20 microscope equipped with a quantum EELS spectrometer and EDX detectors, providing both structural and chemical analyses.

2.4. Thermoelectric properties characterization

Physical properties measurement system (PPMS, Quantum Design) with thermal transport option (TTO) is powerful for investigating the low-temperature (< 400 K) thermoelectric properties S, ρ, κ. Different from traditional ZEM-3 for S, ρ and laser-flash-method for κ using two different-size samples to meet each measurement requirement, PPMS can achieve the three parameters in one sample in one direction to avoid the errors in choosing samples. As thermal conductivity $\kappa=K(L/A)$ and resistivity $\rho=R(A/L)$ are calculated from the thermal conductance K, resistance R, sample length L and section area A, the calculated ZT value ($S^2T/\rho\kappa$) is independence of L/A, avoiding the errors of sample geometries. Steady-state measurement is preferred for measuring the thermal conductivity. To make sure the steady-state measurement in PPMS-TTO at each test temperature, the single-timed-mode are chose instead of the default continuous-mode, even though much longer measuring time has to be taken for single-timed-mode. The dominant errors in PPMS-TTO for estimating ZT come from the thermal conductivity when correcting the heat loss. The mostly-used commercial p-type $Bi_{0.5}Sb_{1.5}Te_3$ ingot are used to calibrate the heat loss, which shows comparable results with the values given by the company and other reported values in literatures by ZEM and laser-flash-method (listed in Table S1, Fig. S1). Each measuring errors of S, ρ, κ and ZT are generated from the measuring systems. The thermoelectric measurements of our nanobulk samples were taken along the disc-plane direction that was perpendicular to the SPS-pressing direction and that of ingot samples were along the cleavage direction. The Hall coefficient (R_H) was measured in the PPMS with AC transport option by sweeping the magnetic strength up to 2 T in both positive and negative directions. The Hall carrier density n was estimated to be −1/

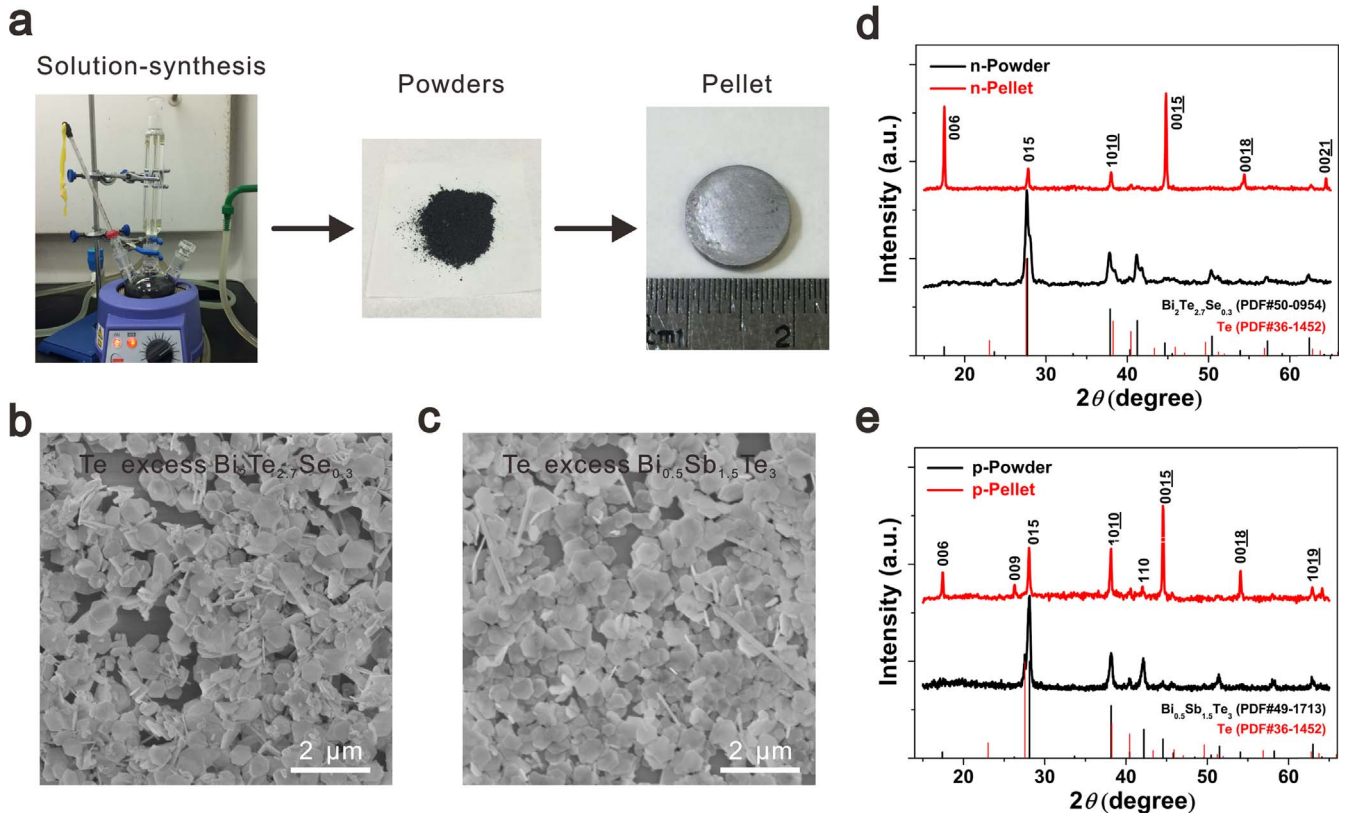

Fig. 1. (a) Schematic representation of the bottom-up approach to nanostructured bulk pellet in two steps: solution-synthesis to get powders and spark plasma sintering process to achieve bulk pellets. **(b)(c)** Scanning electron micrographs of Te-$Bi_2Te_{2.7}Se_{0.3}$ and Te-$Bi_{0.5}Sb_{1.5}Te_3$ mixtures respectively, revealing the nanowires and nanoplates morphology in the powders. **(d)(e)** X-ray diffraction patterns of powders and pellets of the n-Nano and p-Nano samples respectively, showing the distinct Te phase in the powders but undetectable in pellets.

(eR_H), where e is the elementary charge.

3. Results and discussions

3.1. Bottom-up approach for nanostructured bulk thermoelectric materials

Basing on our previous experiments on the wet-chemical synthesis of pnictogen chalcogenide nanocrystals like Bi_2Se_3 [44], p-type $Bi_xSb_{2-x}Te_3$ [28] and n-type $Bi_2Te_{3-y}Se_y$ [25,26], we introduced excess tellurium in the chemical synthesis of Te-$Bi_2Te_{2.7}Se_{0.3}$ and Te-$Bi_{0.5}Sb_{1.5}Te_3$ mixtures. As displayed in Fig. 1a, the chemical synthesis is carried out in a flask heated by electrothermal mantel for 3 h, producing black precipitates in the solution. Powders are collected from the precipitates, and are finally produced into bulk pellets by SPS process (Fig. 1a). The precipitates consist of nanoplates and nanowires as shown in the SEM images of solution-grown Te-$Bi_2Te_{2.7}Se_{0.3}$ and Te-$Bi_{0.5}Sb_{1.5}Te_3$ mixtures (Fig. 1b and c). Solution-grown Te nanocrystals in our growth conditions usually reveal the nanowire-shape, while $Bi_2Te_{2.7}Se_{0.3}$ and $Bi_{0.5}Sb_{1.5}Te_3$ are nanoplate-shapes [26,28], as proved by the localized Raman spectra of those nanowires and nanoplates (Fig. S2). The XRD spectra of those collected powders also reveal that solution-derived Te-$Bi_2Te_{2.7}Se_{0.3}$ and Te-$Bi_{0.5}Sb_{1.5}Te_3$ are the mixtures of Te and $Bi_2Te_{2.7}Se_{0.3}$, and $Bi_{0.5}Sb_{1.5}Te_3$ respectively (Fig. 1d and e). During the SPS process at temperature 460 °C (above the melting temperature of Te, which is ~450 °C) and pressure 60 MPa, the excess Te are liquefied and can be expelled out from the graphite die together with other eutectic mixtures (see Fig. S3). As shown in Fig. 1d and e, no Te-related peaks can be clearly identified from the XRD spectra of the final SPS derived bulk pellets, though tiny remaining Te phase in the n-type pellets can be found by TEM characterization as shown below. Compared with powder mixture samples, SPS derived pellets have much sharper peaks and enhanced peaks of (006), (0015) and (0018), demonstrating that those nanoplates have reorientation trends into the disc plane perpendicular to the press direction, which is also observed in our previous reports [25,26,28].

3.2. Thermoelectric properties

Fig. 2 shows the thermoelectric properties of our typical nanobulk samples and the commercial ingots in the temperature region 5–370 K, measured by PPMS-TTO single-timed-mode. The widely-used commercial n-Ingot and p-Ingot samples are used as calibration for PPMS system and comparison for our nanobulk samples as well, whose ZT peak values are ~1.0 at around 325–350 K, in agreement with other reports on commercial ingots [6,9,20]. The electrical resistivity of all the samples increases with temperature, which reveals their metallic behavior (Fig. 2a). The electrical resistivity of our n-Nano and p-Nano is higher than that of n-Ingot and p-Ingot respectively, which can be ascribed to more scattering introduced by nanostructures in the nanobulk samples. The Seebeck coefficient of p-Nano is close to that of p-Ingot at low and high temperatures while the Seebeck coefficient of n-Nano is slightly lower than that of n-Ingot one (Fig. 2b). As shown in Fig. 2c and its inset, the thermal conductivity of our n-Nano and p-Nano samples are significantly lower than that of commercial n-Ingot and p-Ingot, especially at lower temperature (< 50 K). Most importantly, as the temperature increases from 325 to 370 K, the thermal conductivity of n-Ingot and p-Ingot starts to increase while that of n-Nano and p-Nano still decreases (Fig. 2c), leading to enhanced ZT values for the nanobulk samples at higher temperature region (Fig. 2d). As shown in Fig. 2d, the ZT of our p-Nano sample is close to that of p-Ingot below 275 K, but higher than that of p-Ingot from 300 to 370 K. On the other hand, the ZT of our n-Nano sample is slightly lower than

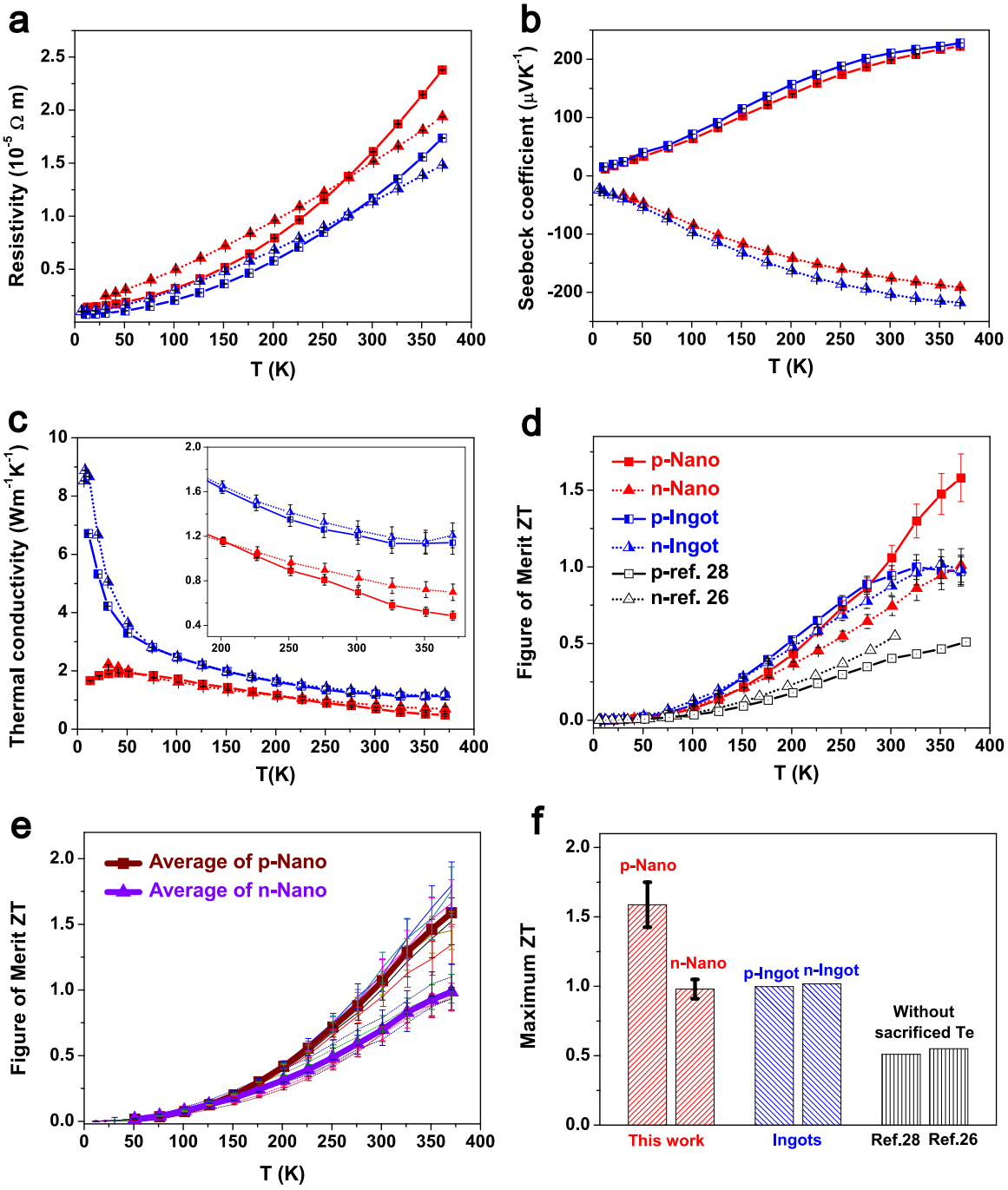

Fig. 2. Temperature dependence of **(a)** electrical resistivity, **(b)** Seebeck coefficient, **(c)** thermal conductivity, and **(d)** the figure of merit (ZT) for our nanobulk samples (n-type n-Nano and p-type p-Nano) and commercial ingots (n-type n-Ingot and p-type p-Ingot). The inset in (c) corresponds to the enlarge region of (c) in the range 200–370 K. (a)(b)(c)(d) share the same annotation as shown in (d). **(e)** ZT average of all the corresponding measured n-Nano and p-Nano samples. **(f)** The maximum ZT of our nanobulk samples in this work (in 5–370 K range) comparing with commercial ingots and our previous work without liquid-phase-sintering process by sacrificed Te (p-type in Ref. [28] and n-type in Ref. [26], their temperature dependence of ZT are also shown in (d)).

that of n-Ingot below 350 K, but it starts to overcome that of n-Ingot at 370 K (Fig. 2d). What's more, both p-Nano and n-Nano samples in this work have much higher ZT compared with our previous samples without sacrificed Te to enable LPS process [26,28], as shown in Fig. 2d. Fig. 2e shows the average ZT values of p-Nano and n-Nano samples based on all the measured samples, and the other corresponding thermoelectric properties are listed in Fig. S4 and Fig. S5 respectively. As shown in Fig. 2f, the average maximum ZT values are calculated to be as high as 0.98 ± 0.07 (ZT ranging from 0.93 to 1.1) for n-Nano at 370 K and 1.59 ± 0.16 (ZT ranging from 1.35 to 1.80) for p-Nano at 370 K, which are about 2 times and 3 times higher respectively than that of our previous samples without using the LPS process [26,28]. Our p-Nano samples have ~60% increase in ZT compared to p-Ingot sample, while our n-Nano samples are also comparable with the n-Ingot sample.

Generally speaking, Bi_2Te_3-based commercial ingots always suffer from the crack problem along their cleavage plane, which is a disadvantage for device fabrication and integration. Introducing polycrystalline structures with smaller grains is a common way to improve materials' fracture resistance, which is also recently proved in nanostructured $Bi_{0.5}Sb_{1.5}Te_3$ samples by melt spinning combined with plasma-activated sintering [45]. During the cutting process of bulk

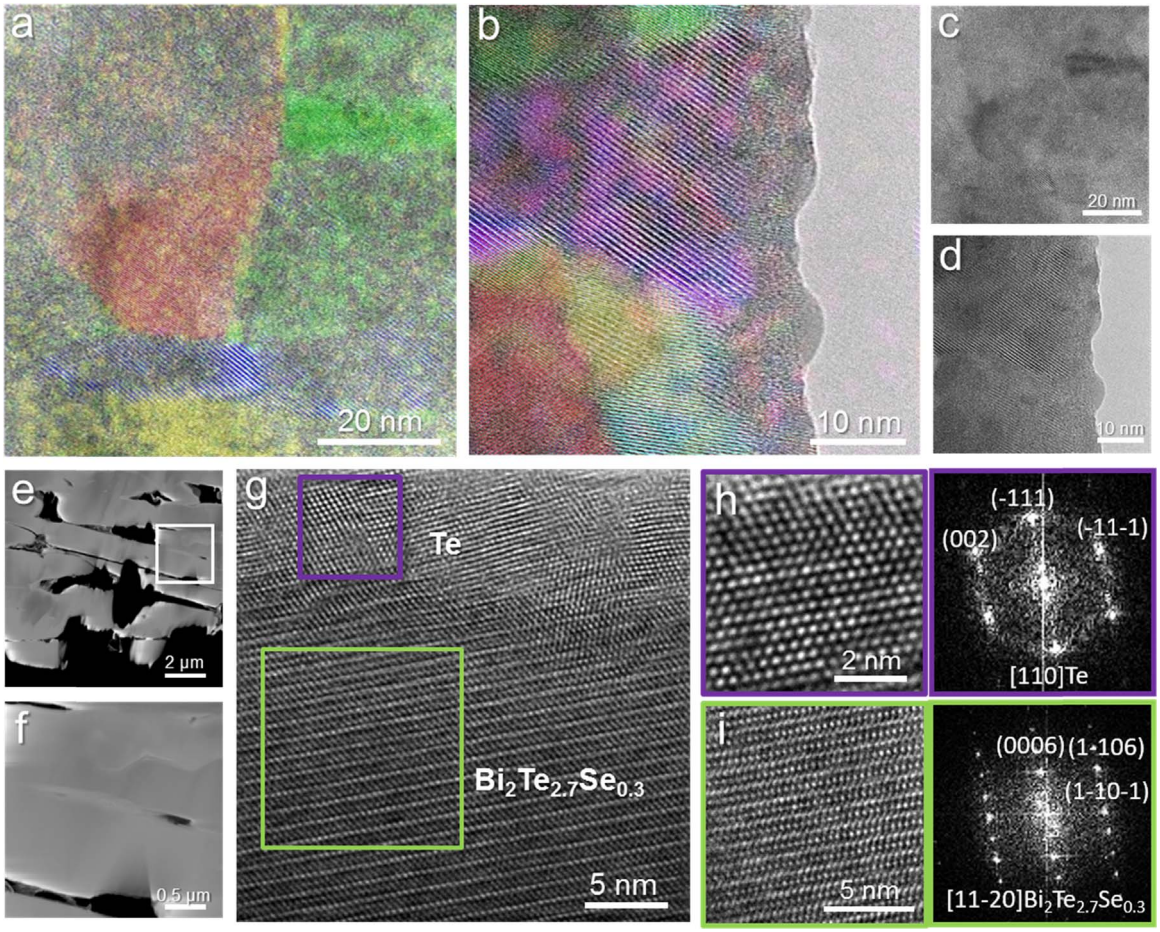

Fig. 3. TEM characterizations of the n-Nano bulk samples. (a)(b) HRTEM combined with phase filtered coloured images of n-Nano bulk samples in planar view, revealing various nanograins with different orientations. (c)(d) The corresponding original HRTEM images of (a)(b), respectively. (e) Cross-section low magnification HAADF STEM image of n-Nano. Cracks are found in grain boundaries during the thinning process of TEM samples. (f) Magnified detail of the white framed area in (e). (g) Cross-section HRTEM image of the n-Nano sample near a grain boundary, showing the existence of segregated Te phase at the grain boundary. (h)(i) Zooming HRTEM details of crystallographic phase of Te and $Bi_2Te_{2.7}Se_{0.3}$ respectively in the framed areas of (g), along with their corresponding indexed power spectra.

materials, we did find that the annoying crack problem is quite common in commercial ingots (see Fig. S6) but not happened in our nanobulk samples. Comparing with the large-size grains in commercial ingots, micrometer scale of grains in our nanobulk samples are demonstrated by the SEM images (Fig. S7). Thus, these observations may indicate that the mechanical strength of our nanobulk samples are enhanced, though further mechanical bending or compressing test are still needed to confirm this issue.

3.3. Electron microscopy characterizations

To understand the mechanism of low thermal conductivity in the n-Nano and p-Nano samples, their microstructures were studied by SEM (Fig. S7) and TEM (Fig. 3 and Fig. 4) as well, taken on both cross-section and planar view. As revealed in TEM images (Figs. 3a-d and 4a-d), nanosized grains with different orientations are the most common features in both n-Nano and p-Nano samples. These nanograins are highly crystalline and have clean interfaces between boundaries, as shown in Fig. 3a-d and Fig. 4a-c. As shown in Fig. 3g, i and Fig. 4c-d, the typical high resolution TEM (HRTEM) images and the corresponding fast Fourier transform (FFT) indexed power spectra of n-Nano and p-Nano samples agree well with the cell parameters of $Bi_2Te_{2.7}Se_{0.3}$ and $Bi_{0.5}Sb_{1.5}Te_3$, respectively. For n-Nano samples, most of the regions are composed of the $Bi_2Te_{2.7}Se_{0.3}$ phase, as revealed by energy dispersive X-ray spectroscopy (EDX) data (Fig. S8). In addition, separated Te phases are sporadically observed between boundaries, like the regions shown in Fig. 3e-f. As the HRTEM image shown in Fig. 3g-h, sporadic Te phase exists in the boundaries between different grains. However, we didn't find segregated Te phase in the p-Nano samples, and found that most of the regions are the intended $Bi_{0.5}Sb_{1.5}Te_3$ phase (Fig. S9). For p-Nano samples, segregation phenomenon of constituents is also observed by elemental mapping of the extracted Sb and Te constituents using electron energy loss spectroscopy (EELS), as shown in Fig. 4e-h. Because the characteristic EELS of Sb and Te involves overlapping between each other in some energy region, the extracted main components of the Sb and Te spectra may have deviation from pure elements (Fig. S10), but they are related to actual features of the composition distribution in the compound. We noted that extracted Te signal mainly follows the shape of the crystals, while extracted Sb signal is segregated to certain area, mostly in grain boundaries, as highlighted in the stacked mapping image in Fig. 4h. The Sb-enrich phenomenon may ascribe to the thermodynamic factor that Bi elements have great trend to aggregate into the liquid phase according to the Bi-Sb binary phase diagram. The interface and grain boundaries in our solution-derived nanobulk are drastically different than the melt-spinning composite using the similar LPS process, in which dense dislocations are the dominant defects attributed responsible for lattice thermal conductivity reduction [9].

3.4. Reduction of the lattice thermal conductivity

Reducing the thermal conductivity κ is a big advantage of nanos-

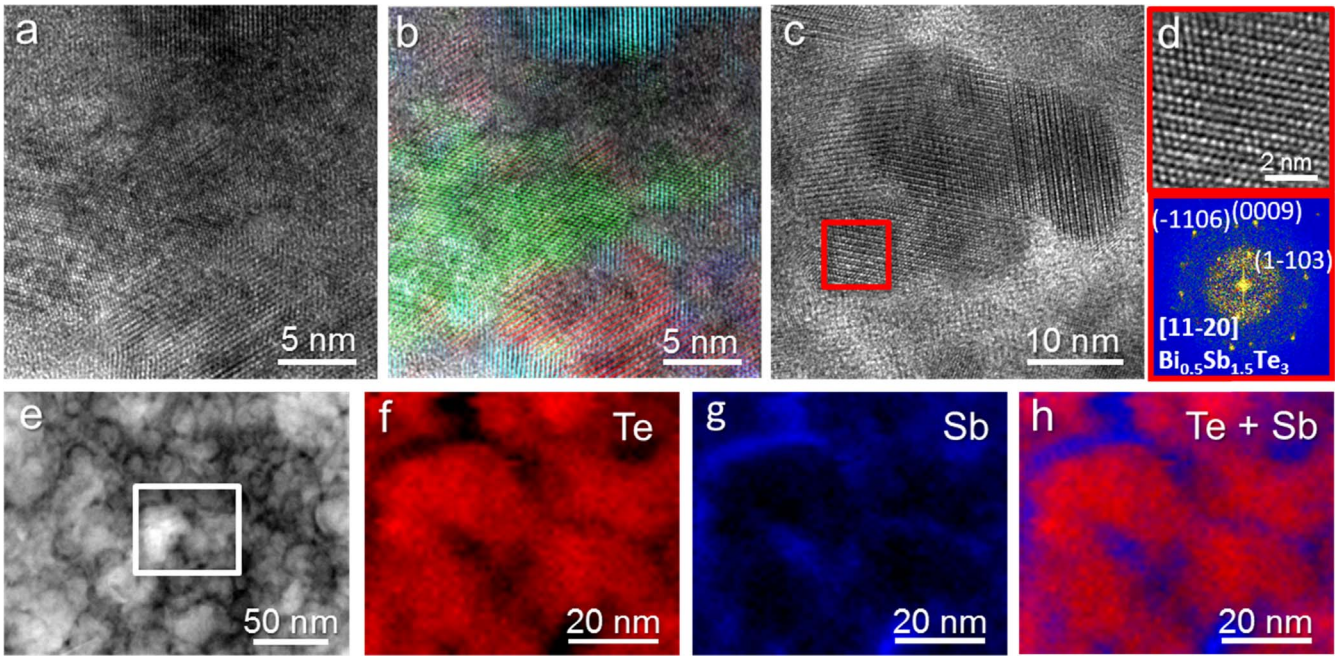

Fig. 4. TEM characterizations of the p-Nano bulk samples. (a)(b) HRTEM combined with phase filtered coloured images of the p-Nano bulk sample in cross-section view, showing nanograins with different orientations. (c) HRTEM image of the p-Nano in another region. (d) Enlarged HRTEM details of the crystallographic phase of $Bi_{0.5}Sb_{1.5}Te_3$ in the red framed area of (c), along with the corresponding indexed power spectrum. (e) Low magnification HAADF image of the p-Nano sample in cross-section view. (f)(g) The EELS elemental mapping of extracted Te and Sb signals, respectively, in the white framed region of (e). (h) Overlay of the extracted Te and Sb elemental maps, showing Sb-enriched regions in some boundary areas.

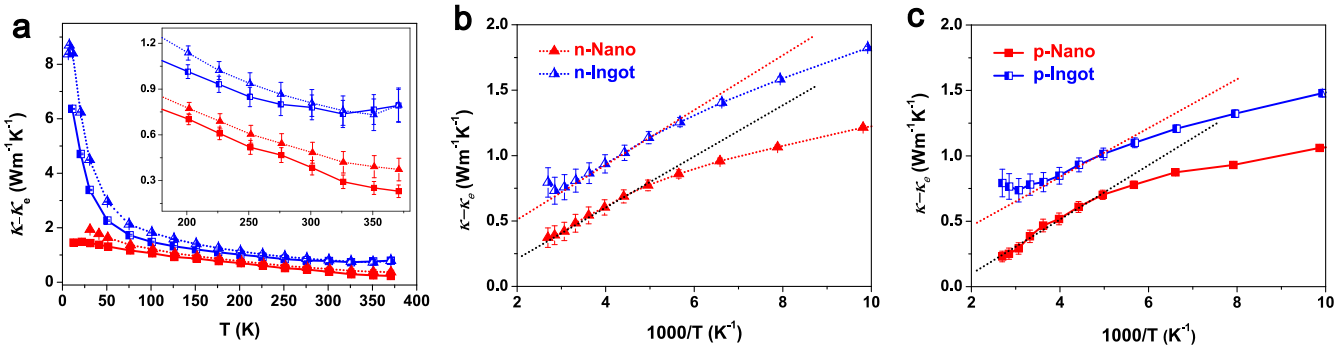

Fig. 5. (a) Temperature dependence of lattice thermal conductivity (κ_l), which are calculated by subtracting the electronic thermal conductivity (κ_e) from the total thermal conductivity. The inset corresponds to the enlarge region of (a) in the range 200–370 K. The ($\kappa - \kappa_e$) vs 1000/T plots of (b) n-Nano vs n-Ingot, and **(c)** p-Nano vs p-Ingot. From 200 K to 370 K, both n-Nano and p-Nano samples show the 1/T temperature dependence of ($\kappa - \kappa_e$), which is due to the dominant phonon-phonon scattering in *Umklapp* process. For commercial ingots, the bipolar effects start to contribute to the total thermal conductivity for T > 300 K, which leads to the increase of ($\kappa - \kappa_e$) at higher temperature. All the data are derived from the Fig. 2, and share the same annotation as shown in Fig. 2d.

tructuring process for improving ZT values [46]. Usually, the electronic thermal conductivity $\kappa_e$and lattice thermal conductivity κ_l are in general the two core contributions to the total thermal conductivity. However at higher temperatures the bipolar contribution (κ_B) due to both electrons and holes [46], plays a significant role. The reduction of this component, as we show later, can be notable already at room temperature. We determined the κ_l by subtracting κ_e from the total thermal conductivity (ignoring the bipolar contribution firstly), as displayed in Fig. 5a. The κ_e was estimated according to the Wiedemann-Franz lawκ_e=LT/ρ, where the Lorenz number L was calculated using an approximation equation L=1.5+exp (-|S|/116) (where L is in the unit 10^{-8} W Ω K^{-2} and S in μVK^{-1}) [47], as demonstrated in Fig. S11. The values of L at 300 K were calculated to be 1.68×10^{-8}, 1.66×10^{-8}, 1.72×10^{-8}, 1.67×10^{-8} W Ω K^{-2} for p-Nano, p-Ingot, n-Nano, n-Ingot respectively. The reduction of κ_l is noticeable for our n-Nano and p-Nano samples compared to the commercial ingots, especially in the low temperature region (Fig. 5a). For temperatures less than 50 K, the large reduction of κ_l in nanobulk samples compared to commercial ingots can be ascribed to the size effects when the mean-free path of phonons is limited by the external boundaries and imperfections [48]. At room temperature 300 K, the κ_l of p-Nano (0.38 W m^{-1} K^{-1}) is about 2 times smaller than the p-Ingot one (0.78 $Wm^{-1}K^{-1}$), and the κ_l of n-Nano (0.48 W m^{-1} K^{-1}) is also much smaller than the n-Ingot one (0.81 W m^{-1} K^{-1}). To gather a general understanding it could be noted that κ_l can be expressed as a sum of contributions from different frequencies which, for an isotropic material can be simply written as [9,48]:

$$\kappa_l = \int \kappa_s(\omega)d\omega = \int \frac{1}{3} C_p(\omega)\nu(\omega)l(\omega)d\omega$$

where $\kappa_s(\omega)$, $C_p(\omega)$, $\nu(\omega)$, $l(\omega)$ are the spectral lattice thermal conductivity, spectral heat capacity of phonons, phonon-group velocity, phonon mean-free path respectively. The $l(\omega)$ depends mainly on three contributions, *Umklapp* processes, scattering from point defects and from the boundaries, each of these contributions being more significant at different frequencies [8,9]. Comparing with commercial ingots with

large-size grains, our nanobulk samples have a larger concentration of nanosized grains and boundaries as observed in TEM (Figs. 3 and 4) and micrometer scale of grains and boundaries observed in SEM (Fig. S7). In addition, other lattice defects such as segregated phase between boundaries (Te-phase in n-Nano, Sb-enrich region in p-Nano), strain, dislocations and impurity point-defects can also contribute to different phonon scattering processes. Thus, comparing with commercial ingots, the extra reduction of κ_l in our nanobulk samples are ascribed to these phonon scattering over a wide spectrum of frequencies. As the densities of our nanobulk samples are around 10% lower than commercial ingots, the porosity structures also contribute to the reduction of κ_l as well as the increase of resistivity ρ.

3.5. Suppression of the bipolar thermal conductivity

At high temperature region (T > θ, θ as Debye temperature), the phonon scattering by *Umklapp* mechanism leads to a T^{-1} temperature dependence of thermal conductivity, while bipolar effect contributes to the increase of thermal conductivity at higher temperature (> 300 K). As the Debye temperature of Bi_2Te_3-based materials is around 145 K [49], the T^{-1} linear fitting in Fig. 5b-c (the graph of $(\kappa - \kappa_e)$ vs 1000/T) is made from 200 K. The $\kappa - \kappa_e$ of commercial ingots is a combination of *Umklapp* process (T^{-1} dependence) and bipolar effects from 200 K. For commercial ingots, the bipolar effects start to overcome the *Umklapp* process when temperature increases above 325–350 K, leading to the increase of thermal conductivity. However, our n-Nano and p-Nano samples only exhibit the linear behavior with T^{-1} dependence (from *Umklapp* process) from 200 to 370 K, indicating the suppression of bipolar thermal conductivity. The suppression of bipolar effects has been realized by several strategies, such as increasing the majority carrier density [17,46], enlarging the bandgap [46,50], building up interfacial potential energy barrier through nanostructuring boundaries [6,49], and presenting selective scattering of minority carriers and thus limiting their conductivity [51]. For our n-Nano samples, the increase of carrier density (Fig. 6b), the existence of nanosized grain and grain boundaries and segregated Te phase between boundaries can all contribute to the suppression of bipolar effect. Although the carrier density of p-Nano is nearly the same as p-Ingot, segregated Sb-enrich regions between boundaries and other nanostructured boundaries can also contribute to the extra potential barrier in those interfaces for selective scattering of minority carriers. With the phonon scattering from various imperfections and suppression of bipolar effects, the κ_l values of our n-Nano and p-Nano samples are as low as 0.37 and 0.23 W m^{-1} K^{-1} at 370 K respectively, much lower than the n- and p-Ingot values (0.79 W m^{-1} K^{-1}).

3.6. Preserving the power factor

Fig. 6a shows the temperature dependence of power factors (*PF*) of our nanobulk samples comparing with that of commercial ingots. The *PF* of n-Nano, p-Nano, n-Ingot, p-Ingot at 300 K (370 K) are 2.0(1.9), 2.5(2.1), 3.6(3.2), 3.8(3.0) mW m^{-1} K^{-2}, respectively. Although the *PF* of our nanobulk samples are still lower than that of the commercial ingots, they are much higher than the values reported in most of other solution-derived nanocomposites with *PF* < 1.8 mW m^{-1} K^{-2} in all temperature region [21–23,25,26,28–30,33–35]. Calculated from Hall measurements, the carrier densities *n* of the ingot and nanobulk samples are in the range 1–3×10^{19} cm^{-3} and nearly independent of the temperature (Fig. 6b). Generally, the Seebeck coefficient shows strong dependence on the carrier density [2]: $S \propto n^{-2/3}$. The carrier density in p-Nano is nearly the same with p-Ingot (~1.45×10^{19} cm^{-3} at 300 K for both), which agrees well with their nearly close Seebeck coefficient. On the other hand, the carrier density of n-Nano (2.47×10^{19} cm^{-3}) is higher than that of n-Ingot (1.83×10^{19} cm^{-3}) at 300 K, which can be the reason for the reduction of the Seebeck coefficient in n-Nano. Fig. 6c demonstrates the temperature dependence of the charge-carrier mobility μ, calculated with the formula $\mu = 1/(n\rho e)$. Compared with ingots, the decrease of μ in nanobulk samples is mainly due to additional electron scattering from interfacial charge potential and boundaries, which is the main reason for the lower power factor compared with ingot samples. Considering so many imperfection introduced for the greatly reduction of κ, the *PF* in our nanobulk samples is well preserved, though a bit lower than the ingot samples.

3.7. Liquid-phase-sintering

Liquid-phase-sintering is effective for densification, boundaries connecting and interface engineering [43]. In our SPS process, the excess Te is liquefied when the sintering temperature is higher than the melting temperature of Te (450 °C). Some eutectic compositions (p-type $Bi_{0.5}Sb_{1.5}Te_3$ and n-type $Bi_2Te_{2.7}Se_{0.3}$) are also liquefied together with Te. Those liquid mixtures have high mass-diffusivity, which can quickly penetrate into those grain boundaries, facilitating the grain connecting, coarsening and rearrangement for better electrical transport. Compared with our previous results without adding excess Te in the solution-synthesis process [26,28], nanobulk samples in this work have much higher power factor besides having much lower lattice thermal conductivity (Fig. S12). The existence of liquid-phase also facilitates the dispersion of nanosized solids in the liquid, especially for our solution-derived nanoplates with smaller crystalline size, which leads to a larger concentration of nanosized grains and boundaries as observed in TEM for the reduction of lattice thermal conductivity. The microstructures of remaining Te phase in n-Nano and Sb-enrich regions in p-Nao between grains can be the trace left after most of liquid Te are expelled out, which leads to the charge barrier for the suppression of bipolar effect. As shown in XRD (Fig. 1d-e), the peak ratio I_{006}/I_{015} of n-Nano is much higher than that of p-Nano, indicating much stronger reorientation trends into the disc plane for n-Nano

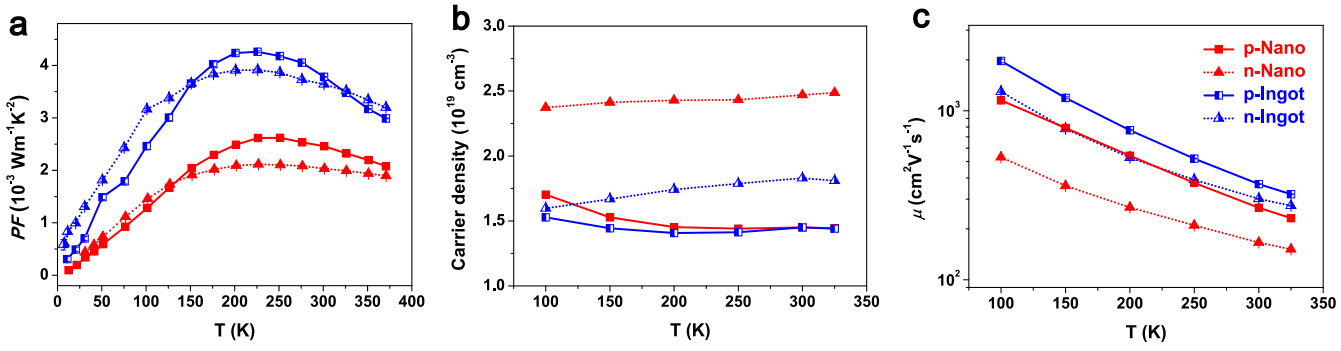

Fig. 6. Temperature dependence of **(a)** power factor *PF* (S^2/ρ), **(b)** charge density *n*, and **(c)** charge-carrier mobility μ. The samples are the same as shown in Fig. 2. The μ are calculated by the formula $\mu = 1/(n\rho e)$, where the charge density *n* are determined by the Hall measurements and the electrical resistivity *ρ* is from the data in Fig. 2a. All the figures share the same annotation as shown in (c), which are the same as Fig. 2d.

samples. The stronger reorientations of n-Nano samples prohibits the completely remove of excess Te phase for optimizing the n and also leads to much higher κ_l comparing with p-Nano, which limits the thermoelectric performance of n-Nano samples. Besides the difference in anisotropy, the higher κ_l in n-Nano $Bi_2Te_{2.7}Se_{0.3}$ comparing with p-Nano $Bi_{0.5}Sb_{1.5}Te_3$ can also ascribe to the relatively lower point defect scattering from the arrangements of elements [15]. Developing the LPS process by adding other easy-liquefied materials like In, Sn, Se and other alloys can be used to further improve the power factor for high-ZT solution-derived nanocomposites.

4. Conclusion

We have introduced the liquid-phase-sintering process to the bottom-up approach for the nanostructuring design of both n-type $Bi_2Te_{2.7}Se_{0.3}$ and p-type $Bi_{0.5}Sb_{1.5}Te_3$ bulk nanocomposites. The average maximum ZT values of these nanobulk samples at 370 K reach up to 1.59 ± 0.16 for p-type $Bi_{0.5}Sb_{1.5}Te_3$ and 0.98 ± 0.07 for n-type $Bi_2Te_{2.7}Se_{0.3}$, which is higher and comparable with the corresponding p-type and n-type commercial ingots, respectively. By introducing liquid-phase in the sintering process, grains are better connected for preserving the power factor while plenty of nanosized grain and boundaries are generated for reducing the lattice thermal conductivity, which leads to the achievement of high thermoelectric performance in our solution-derived nanocomposites. Segregated phases are also observed in our nanobulk samples, which leads to the suppression of bipolar thermal conductivity. We proved that a great ZT enhancement can be realized by this cost-effective, facile and scalable chemical bottom-up approach. Considering the facility and full of variety in the chemical synthesis of nanomaterials, there is huge potential and great prospect for bottom-up approaches to further improve the thermoelectric performance by designing new nanostructured materials.

Acknowledgment

Q.X. gratefully thanks Singapore National Research Foundation via a Fellowship grant (NRF-RF2009-06) and an Investigator ship grant (NRF-NRFI2015-03), Ministry of Education via a tier2 grant (MOE2012-T2-2-086) and Nanyang Technological University via a start-up grant support (M58110061). F.J.B, M.d.l. M and J.A acknowledge the funding from the Generalitat de Catalunya 2014 SGR 1638 and the Spanish MINECO project e-TNT (MAT2014-59961-C2-2-R). ICN2 acknowledges support from the Severo Ochoa Program (MINECO, Grant SEV-2013-0295). Q.Y. thanks Singapore A*STAR Pharos program SERC 1527200022. D.P. acknowledges support from Singapore Ministry of Education, Singapore Academic Research Fund Tier-1 (project SUTDT12015005).

Appendix A. Supporting information

Supplementary data associated with this article can be found in the online version at doi:10.1016/j.nanoen.2016.10.056.

References

[1] L.E. Bell, Science 321 (2008) 1457–1461.
[2] G.J. Snyder, E.S. Toberer, Nat. Mater. 7 (2008) 105–114.
[3] A.J. Minnich, M.S. Dresselhaus, Z.F. Ren, G. Chen, Energy Environ. Sci. 2 (2009) 466–479.
[4] C.J. Vineis, A. Shakouri, A. Majumdar, M.G. Kanatzidis, Adv. Mater. 22 (2010) 3970–3980.
[5] K. Biswas, J. He, Q. Zhang, G. Wang, C. Uher, V.P. Dravid, M.G. Kanatzidis, Nat. Chem. 3 (2011) 160–166.
[6] B. Poudel, Q. Hao, Y. Ma, Y. Lan, A. Minnich, B. Yu, X. Yan, D. Wang, A. Muto, D. Vashaee, X. Chen, J. Liu, M.S. Dresselhaus, G. Chen, Z. Ren, Science 320 (2008) 634–638.
[7] R.J. Mehta, Y.L. Zhang, C. Karthik, B. Singh, R.W. Siegel, T. Borca-Tasciuc, G. Ramanath, Nat. Mater. 11 (2012) 233–240.
[8] K. Biswas, J. He, I.D. Blum, C.I. Wu, T.P. Hogan, D.N. Seidman, V.P. Dravid, M.G. Kanatzidis, Nature 489 (2012) 414–418.
[9] S. Il Kim, K.H. Lee, H.A. Mun, H.S. Kim, S.W. Hwang, J.W. Roh, D.J. Yang, W.H. Shin, X.S. Li, Y.H. Lee, G.J. Snyder, S.W. Kim, Science 348 (2015) 109–114.
[10] X. Yan, B. Poudel, Y. Ma, W.S. Liu, G. Joshi, H. Wang, Y. Lan, D. Wang, G. Chen, Z.F. Ren, Nano Lett. 10 (2010) 3373–3378.
[11] D. Wu, Y. Pei, Z. Wang, H. Wu, L. Huang, L.-D. Zhao, J. He, Adv. Funct. Mater. 24 (2014) 7763–7771.
[12] W. Xie, J. He, H.J. Kang, X. Tang, S. Zhu, M. Laver, S. Wang, J.R. Copley, C.M. Brown, Q. Zhang, T.M. Tritt, Nano Lett. 10 (2010) 3283–3289.
[13] Y. Zhao, J.S. Dyck, C. Burda, J. Mater. Chem. 21 (2011) 17049–17058.
[14] J.R. Sootsman, D.Y. Chung, M.G. Kanatzidis, Angew. Chem. Int. Ed. 48 (2009) 8616–8639.
[15] W.M. Yim, F.D. Rosi, Solid-State Electron. 15 (1972) 1121–1140.
[16] J.S. Son, H. Zhang, J. Jang, B. Poudel, A. Waring, L. Nally, D.V. Talapin, Angew. Chem. Int. Ed. 53 (2014) 7466–7470.
[17] L.-P. Hu, T.-J. Zhu, Y.-G. Wang, H.-H. Xie, Z.-J. Xu, X.-B. Zhao, NPG Asia Mater. 6 (2014) e88.
[18] X.B. Zhao, X.H. Ji, Y.H. Zhang, T.J. Zhu, J.P. Tu, X.B. Zhang, Appl. Phys. Lett. 86 (2005) 062111.
[19] W.-S. Liu, Q. Zhang, Y. Lan, S. Chen, X. Yan, Q. Zhang, H. Wang, D. Wang, G. Chen, Z. Ren, Adv. Energy Mater. 1 (2011) 577–587.
[20] L. Hu, H. Wu, T. Zhu, C. Fu, J. He, P. Ying, X. Zhao, Adv. Energy Mater. 5 (2015) 1500411.
[21] Y. Min, J.W. Roh, H. Yang, M. Park, S.I. Kim, S. Hwang, S.M. Lee, K.H. Lee, U. Jeong, Adv. Mater. 25 (2013) 1425–1429.
[22] M. Scheele, N. Oeschler, I. Veremchuk, K.G. Reinsberg, A.M. Kreuziger, A. Kornowski, J. Broekaert, C. Klinke, H. Weller, ACS Nano 4 (2010) 4283–4291.
[23] G.-H. Dong, Y.-J. Zhu, L.-D. Chen, J. Mater. Chem. 20 (2010) 1976–1981.
[24] R.J. Mehta, Y. Zhang, H. Zhu, D.S. Parker, M. Belley, D.J. Singh, R. Ramprasad, T. Borca-Tasciuc, G. Ramanath, Nano Lett. 12 (2012) 4523–4529.
[25] A. Soni, Y. Shen, M. Yin, Y. Zhao, L. Yu, X. Hu, Z. Dong, K.A. Khor, M.S. Dresselhaus, Q. Xiong, Nano Lett. 12 (2012) 4305–4310.
[26] A. Soni, Z. Yanyuan, Y. Ligen, M.K. Aik, M.S. Dresselhaus, Q. Xiong, Nano Lett. 12 (2012) 1203–1209.
[27] G. Zhang, B. Kirk, L.A. Jauregui, H. Yang, X. Xu, Y.P. Chen, Y. Wu, Nano Lett. 12 (2012) 56–60.
[28] C. Zhang, Z. Peng, Z. Li, L. Yu, K.A. Khor, Q. Xiong, Nano Energy 15 (2015) 688–696.
[29] M. Scheele, N. Oeschler, K. Meier, A. Kornowski, C. Klinke, H. Weller, Adv. Funct. Mater. 19 (2009) 3476–3483.
[30] S. Sun, J. Peng, R. Jin, S. Song, P. Zhu, Y. Xing, J. Alloy. Compd. 558 (2013) 6–10.
[31] C. Kim, D.H. Kim, J.T. Kim, Y.S. Han, H. Kim, ACS Appl. Mater. Interfaces 6 (2014) 778–785.
[32] J. Fu, S. Song, X. Zhang, F. Cao, L. Zhou, X. Li, H. Zhang, CrystEngComm 14 (2012) 2159.
[33] Z. Lu, L.P. Tan, X. Zhao, M. Layani, T. Sun, S. Fan, Q. Yan, S. Magdassi, H.H. Hng, J. Mater. Chem. C 1 (2013) 6271–6277.
[34] J.S. Son, M.K. Choi, M.K. Han, K. Park, J.Y. Kim, S.J. Lim, M. Oh, Y. Kuk, C. Park, S.J. Kim, T. Hyeon, Nano Lett. 12 (2012) 640–647.
[35] M.R. Dirmyer, J. Martin, G.S. Nolas, A. Sen, J.V. Badding, Small 5 (2009) 933–937.
[36] Y. Min, G. Park, B. Kim, A. Giri, J. Zeng, J.W. Roh, S.I. Kim, K.H. Lee, U. Jeong, ACS Nano 9 (2015) 6843–6853.
[37] D. Suh, S. Lee, H. Mun, S.-H. Park, K.H. Lee, S. Wng Kim, J.-Y. Choi, S. Baik, Nano Energy 13 (2015) 67–76.
[38] M. Hong, Z.G. Chen, L. Yang, J. Zou, Nano Energy 20 (2016) 144–155.
[39] L. Yang, Z.G. Chen, M. Hong, G. Han, J. Zou, ACS Appl. Mater. Interfaces 7 (2015) 23694–23699.
[40] M. Hong, T.C. Chasapis, Z.G. Chen, L. Yang, M.G. Kanatzidis, G.J. Snyder, J. Zou, ACS Nano 10 (2016) 4719–4727.
[41] M. Hong, Z.-G. Chen, L. Yang, G. Han, J. Zou, Adv. Electron. Mater. 1 (2015) 1500025.
[42] M. Hong, Z.G. Chen, L. Yang, J. Zou, Nanoscale 8 (2016) 8681–8686.
[43] R.M. German, P. Suri, S.J. Park, J. Mater. Sci. 44 (2009) 1–39.
[44] J. Zhang, Z. Peng, A. Soni, Y. Zhao, Y. Xiong, B. Peng, J. Wang, M.S. Dresselhaus, Q. Xiong, Nano Lett. 11 (2011) 2407–2414.
[45] Y. Zheng, Q. Zhang, X. Su, H. Xie, S. Shu, T. Chen, G. Tan, Y. Yan, X. Tang, C. Uher, G.J. Snyder, Adv. Energy Mater. 5 (2015) 1401391.
[46] W. Liu, X. Yan, G. Chen, Z. Ren, Nano Energy 1 (2012) 42–56.
[47] H.-S. Kim, Z.M. Gibbs, Y. Tang, H. Wang, G.J. Snyder, APL Mater. 3 (2015) 041506.
[48] P.G. Klemens, Solid State Phys. 7 (1958) 1–98.
[49] P. Puneet, R. Podila, M. Karakaya, S. Zhu, J. He, T.M. Tritt, M.S. Dresselhaus, A.M. Rao, Sci. Rep. 3 (2013) 3212.
[50] L.D. Zhao, H.J. Wu, S.Q. Hao, C.I. Wu, X.Y. Zhou, K. Biswas, J.Q. He, T.P. Hogan, C. Uher, C. Wolverton, V.P. Dravid, M.G. Kanatzidis, Energy Environ. Sci. 6 (2013) 3346–3355.
[51] S. Wang, J. Yang, T. Toll, J. Yang, W. Zhang, X. Tang, Sci. Rep. 5 (2015) 10136.

Dr. Chaohua Zhang is currently a research fellow in the School of Physical and Mathematical Sciences at Nanyang Technological University, Singapore. He received his B.S. degree in physics from Lanzhou University in 2008, and received a Ph.D. degree in physical chemistry under the supervision of Prof. Zhongfan Liu from Peking University in 2013. He joined in Prof. Qihua Xiong's group since 2013. His research is focused on the control growth of 2D materials, synthesis and characterization of thermoelectric materials.

Dr. María de la Mata graduated in Chemistry at Universidad de Oviedo (Spain) in 2009. She obtained her M.Sc. in Materials Science at Universitat Autònoma de Barcelona (UAB). In 2015, obtained her Ph.D. in Materials Science from UAB at Institut de Ciència de Materials de Barcelona (ICMAB-CSIC), under the supervision of Prof. J. Arbiol. She was Post-Doc in the Group of Advanced Electron Nanoscopy (GAeN) at Institut Català de Nanociència i Nanotecnologia (ICN2). In 2016 she has been post-doc at Lund University. In 2015 she was awarded to participate at the 65th Lindau Nobel Laureate Meeting and obtained the IFSM Young Scientist Award at the IMC2014.

Zhong Li received his Bachelor's degree in Mechanical Engineering & Automation from South China University of Technology (SCUT), Guangzhou, China in 2012. He is currently working in Prof. K.A. Khor's group as a project officer at Nanyang Technological University, Singapore. His research interests are in the high-energy processing of materials, especially the synthesis, sintering and characterization of bioceramics intended for orthopedic applications and artificial corneal implants.

Francisco J. Belarre (M.Sc.) graduated in Materials Science Enginery in 2009 and Physics in 2010 at Universitat Autònoma de Barcelona (UAB). He obtained his MSc in Materials Science at Universitat Autònoma de Barcelona (UAB) in 2011. From 2009–2014 he worked as Research Engineer at Institut de Ciència de Materials de Barcelona (ICMAB-CSIC), in its electron microscopy facilities. Since 2015 he is a member of the Electron Microscopy Division at Institut Català de Nanociència i Nanotecnologia (ICN2).

Prof. Jordi Arbiol graduated in Physics at Universitat de Barcelona (UB) in 1997, where he also obtained his Ph.D. (European Doctorate and Ph.D. Extraordinary Award) in 2001 in the field of transmission electron microscopy (TEM) applied to nanostructured materials. He was Assistant Professor at UB. From 2009–2015 he was Group Leader at Institut de Ciència de Materials de Barcelona, ICMAB-CSIC. Since 2013 he is Vice-President of the Spanish Microscopy Society (SME). Since 2015 he is the leader of the Group of Advanced Electron Nanoscopy at Institut Català de Nanociència i Nanotecnologia (ICN2), CSIC and The Barcelona Institute of Science and Technology (BIST). He has been awarded with the 2014 EMS Outstanding Paper Award, the EU40 Materials Prize 2014 (E-MRS), listed in the Top 40 under 40 Power List (2014) by The Analytical Scientist and the PhD Extraordinary Award in 2001 (UB).

Khiam Aik Khor is a professor at School of Mechanical & Aerospace Engineering in Nanyang Technological University (NTU), Singapore, and currently served as the Director of Research Support Office & Bibliometrics Analysis in NTU. He received his PhD degrees from Monash University, Australia. He worked as an Experimental Scientist at the Commonwealth Scientific and Industrial Research Organization (CSIRO) in Melbourne before joining NTU in 1989. He has held a number of academic, research and administrative appointments, such as Deputy Director, Singapore-MIT Alliance (SMA), Singapore Office; Director (Projects) at the National Research Foundation (NRF) of Singapore; Associate Provost (Research), President's Office, NTU. He is also the President, Institute of Materials, East Asia (IoMEA) from 1996. His research focus on nano-bioceramics and nano-composites for artificial cornea implants, orthopedic and dental implants, spark plasma sintering (SPS) of nano-materials and nano-powders (metals and ceramics), thin films, thermal sprayed coatings, thermal barrier coatings (TBC) for aerospace applications and solid oxide fuel cells.

Dario Poletti is Assistant Professor at the Singapore University of Technology and Design (SUTD). He received a double Master degree in Engineering from Politecnico di Milano and Ecole Centrale Paris. He then obtained a Joint Ph.D. in Physics from the National University of Singapore and the Australian National Unversity. He then researched at the Centre for Quantum Technologies, at the Ecole Polytechnique and at the University of Geneva before joining SUTD in 2012. His research focuses on manybody quantum mechanics with applications to energy conversion and transport.

Dr. Beibei Zhu is currently a research fellow in the School of Materials Science and Engineering at Nanyang Technological University, Singapore. She received her B.S. and M.Sc. degrees in Materials Science and Engineering from Southeast University in China. In 2015, she obtained her Ph.D. in Materials Science from UNSW in Australia. Her research is focused on the synthesis and characterization of thermoelectric bulk materials.

Qingyu Yan is currently an associate professor in School of Materials Science and Engineering in Nanyang Technology University. He obtained his BS in Materials Science and Engineering, Nanjing University. He finished his Ph.D. from Materials Science and Engineering Department of State University of New York at Stony Brook. After that, He joined the Materials Science and Engineering Department of Rensselaer Polytechnic Institute as a postdoctoral research associate. He joined School of Materials Science and Engineering of Nanyang Technological University as an assistant professor in early 2008 and became an associate Professor in 2013. Yan's research efforts have been mainly devoted to two areas: (1) advanced electrode materials for energy storage devices; (2) high-efficiency thermoelectric semiconductor.

Qihua Xiong received his B.S. degree in physics from Wuhan University in 1997, and then finished three years graduate studies at the Shanghai Institute of Applied Physics, Chinese Academy of Sciences. He went to the United States in 2000 and received a Ph.D. degree under the supervision of Prof. Peter C. Eklund from The Pennsylvania State University in 2006. After three years postdoctoral experience in Prof. Charles M. Lieber's group at Harvard University, he joined Nanyang Technological University as an assistant professor in 2009 and was promoted to Nanyang Associate Professor in 2014 and Full Professor in 2016. He is a Fellow of Singapore National Research Foundation awarded in 2009. He has been recently awarded the prestigious Nanyang Award for research excellence and the NRF Investigatorship Award by Singapore National Research Foundation. Prof. Xiong's research focuses on light-matter interactions of emergent quantum matter by optical spectroscopy approaches. He recently ventured into the field of 2D layered materials and laser cooling of solids.